

PAPER • OPEN ACCESS

Fabrication of carbon nanotube neuromorphic thin film transistor arrays and their applications for flexible olfactory-visual multisensory synergy recognition

To cite this article: Nianzi Sui *et al* 2025 *Int. J. Extrem. Manuf.* **7** 015503

View the [article online](#) for updates and enhancements.

You may also like

- [Combining electrodermal activity analysis and dynamic causal modeling to investigate the visual-odor multimodal integration during face perception](#)
Gianluca Rho, Alejandro Luis Callara, Francesco Bossi et al.
- [You are as you smell: the effect of odor and breath odor on social acceptance](#)
Alan R Hirsch
- [A neuromorphic model of olfactory processing and sparse coding in the *Drosophila* larva brain](#)
Anna-Maria Jürgensen, Afshin Khalili, Elisabetta Chicca et al.

Fabrication of carbon nanotube neuromorphic thin film transistor arrays and their applications for flexible olfactory-visual multisensory synergy recognition

Nianzi Sui^{1,2,5}, Kaixiang Kang^{1,2,5}, Min Li^{1,2,*}, Dan Zhang^{1,2,3}, Benxiang Li^{1,2,3}, Shuangshuang Shao^{1,2}, Hua Wang⁴ and Jianwen Zhao^{1,2,*} 

¹ School of Nano-Tech and Nano-Bionics, University of Science and Technology of China, No. 398 Ruoshui Road, Suzhou Industrial Park, Suzhou, Jiangsu Province 215123, People's Republic of China

² Key Laboratory of Semiconductor Display Materials and Chips, Division of Nanodevices and Related Nanomaterials, Suzhou Institute of Nano-Tech and Nano-Bionics, Chinese Academy of Sciences, No. 398 Ruoshui Road, Suzhou Industrial Park, Suzhou, Jiangsu Province 215123, People's Republic of China

³ School of the Environment and Safety Engineering, Jiangsu University, Zhenjiang, 212013 Jiangsu, People's Republic of China

⁴ Key Laboratory of Interface Science and Engineering in Advanced Materials of Ministry of Education, Taiyuan University of Technology, NO. 79, Yingze West Main Street, Taiyuan, Shanxi Province 030024, People's Republic of China

E-mail: mli2019@sinano.ac.cn and jwzhao2011@sinano.ac.cn

Received 26 March 2024, revised 1 May 2024

Accepted for publication 14 October 2024

Published 5 November 2024



CrossMark

Abstract

Artificial multisensory devices play a key role in human-computer interaction in the field of artificial intelligence (AI). In this work, we have designed and constructed a novel olfactory-visual bimodal neuromorphic carbon nanotube thin film transistor (TFT) arrays for artificial olfactory-visual multisensory synergy recognition with a very low power consumption of 25 aJ for a single pulse, employing semiconducting single-walled carbon nanotubes (sc-SWCNTs) as channel materials and gas sensitive materials, and poly[[4,8-bis[5-(2-ethylhexyl)-2-thienyl]benzo[1,2-b:4,5-b⁰]dithiophene-2,6-diyl]-2,5-thiophenediyl-[5,7-bis(2-ethylhexyl)-4,8-dioxo-4H,8H-benzo[1,2-c:4,5-c⁰]dithio-phene-1,3-diyl]] (PBDB-T) as the photosensitive material. It is noted that it is the first time to realize the simulation of olfactory and visual senses (from 280 nm to 650 nm) with the wide operating temperature range (0–150 °C) in a single SWCNT TFT device and successfully simulate the recovery of olfactory senses after COVID-19 by olfactory-visual synergy. Furthermore, our SWCNT neuromorphic TFT devices with a high I_{ON}/I_{OFF} ratio (up to 10^6) at a low operating voltage (−2 to 0.5 V) can

⁵ Nianzi Sui and Kaixiang Kang contributed equally to this work.

* Authors to whom any correspondence should be addressed.



Original content from this work may be used under the terms of the [Creative Commons Attribution 4.0 licence](https://creativecommons.org/licenses/by/4.0/). Any further distribution of this work must maintain attribution to the author(s) and the title of the work, journal citation and DOI.

mimic not only the basic biological synaptic functions of olfaction and vision (such as paired-pulse facilitation, short-term plasticity, and long-term plasticity), but also optical wireless communication by Morse code. The proposed multisensory, broadband light-responsive, low-power synaptic devices provide great potential for developing AI robots to face complex external environments.

Supplementary material for this article is available [online](#)

Keywords: carbon nanotube, photosensitive polymers, neuromorphic transistors, olfactory-visual, multisensory synergy recognition

1. Introduction

In the past decades, computers based on the von Neumann architecture have developed considerably, providing great help for mankind to enter the information society. However, the computational data used in von Neumann's traditional architecture needs to be transferred from separate storage units [1, 2]. With the development of technology and the increase in the complexity of information in modern society, the amount of information transferred between the central processor and the memory of von Neumann computer has greatly increased, which leads to a large amount of additional power consumption while the computational efficiency is limited. As the size of the electronic device continues to decrease, the cost and difficulty of its preparation will also increase greatly, so the von Neumann theory has gradually tended to the limit [3, 4].

Unlike the separation of storage and computation under the traditional von Neumann architecture, the synaptic plasticity possessed by the synapses in the brain enables the brain to process information efficiently and operate in parallel, so that information is processed in the human brain in a storage-computation-integrated manner, and this parallel information processing endows the human brain with astonishing computational speeds, ultra-high efficiencies, and ultra-low power consumption. A vast neural network containing more than 10^{15} synapses allows the human brain to perform parallel operations while consuming a small amount of energy (≈ 20 W) [5–7]. There is a strong interest in neuromorphic electronics that mimic the human brain's nervous system with the development of neural computing, which possesses high efficiency in information processing and high complexity in parallel processing of data. Neuromorphic computing will be more advantageous for data-centered applications, such as image recognition and data classification.

The human nervous system interacts with the outside world through physical contact (vision, hearing, somatosensory, etc) in response to changes in the surrounding ecological and social environments, which is mainly realized by the human sensory system. In recent years, the human sensory organs have been simulated in different ways in an effort to mimic, reproduce, and even surpass the human brain's ability to perform critical complex tasks such as decision-making, reasoning, and learning. For example, Wang *et al* used the heterogeneous structure formed between PbS quantum dots and organic semiconductors to simulate visual synapses and achieved not

only comprehensive image recognition, learning, and data analysis, but also accelerated image preprocessing effects at wide wavelengths beyond the human visual range [8]. In addition, Choudhry *et al* proposed an artificial chemosensory neuron synapse based on ionic gels and ionic liquids that mimicked the neurotransmitter release [9].

However, most synaptic transistors can only simulate a single sense, whereas multiple senses are often required in the face of a complex and changing external environment, making the development of multimodal synaptic transistors particularly important [10–12]. Currently, multimodal synaptic systems usually require different sensors to be connected to a separate synaptic device, and such a complex structure and preparation process are not conducive to further applications [13]. Single-walled carbon nanotubes (SWCNTs) with their unique one-dimensional tubular structure, high specific surface area, and excellent mechanical, electrical, thermal, and chemical properties, are capable of responding sensitively to a wide range of gases at room temperature, making them an ideal channel material for the construction of high-performance gas-sensitive transistors [14–21]. Nevertheless, due to the high transparency of carbon nanotube films, SWCNT synaptic devices have limited light absorption and cannot effectively mimic visual functions without modification of any other photosensitive materials. There are a number of ways to achieve or improve the photoresponse of synaptic devices, such as the use of photoresponsive channel materials, or the addition of photosensitive materials to the channels or dielectric layers of the transistors [22–25]. Generally, the structures of organic polymer photoelectric materials are easy to design, modify, and synthesize. For example, poly[[4,8-bis[5-(2-ethylhexyl)-2-thienyl]benzo[1,2-b:4,5-b']dithiophene-2,6-diyl]-2,5-thiophenediyl-[5,7-bis(2-ethylhexyl)-4,8-dioxo-4 H,8 H-benzo[1,2-c:4,5-c']dithiophene-1,3-diyl]] (PBDB-T), a semiconductor material commonly used in organic photovoltaics (OPVs) and organic thin film transistors (OTFTs), shows excellent photoelectric properties with the high stability even at high temperatures [26–28]. More importantly, it is compatible with SWCNT TFT technologies. Therefore, organic polymer photoelectric materials can be acted as one of the ideal photosensitive materials to modify SWCNT TFTs for constructing large-area flexible SWCNT optoelectronic and gas-sensitive TFT devices.

In this study, we have used SWCNTs with high sensitivity gas response as channel materials and gas-sensitive materials,

and PBDB-T as the photosensitive layer, to construct high-performance SWCNT synaptic TFTs with high I_{On}/I_{Off} ratios of 1×10^6 at low operating voltages (-2 V to 0.5 V) and power consumption as low as 25 aJ per light pulse, which can simulate olfactory and visual (280 – 650 nm) synaptic functions in a single device over the wide operating temperature range (0 – 150 °C). Based on these excellent characteristics, the proposed multisensory synaptic transistors not only successfully realize Morse code wireless optical communication, but also simulate the bimodal recovery training process after a virus-induced olfactory loss by taking advantage of olfactory-visual coordination. This research on monosynaptic transistor devices integrating multiple senses lays the foundation for the subsequent development of artificial intelligence (AI) to face more complex environments.

2. Experimental section

2.1. Materials

Arc discharge SWCNTs (P2, the diameter of SWCNTs from 1.2 nm to 1.6 nm) were purchased from Carbon Solution. Poly (9,9-dioctylfluorene) derivatives (PFIID) ($M_n = 6\,527$, $M_w = 10\,686$) and PBDB-T was purchased from Sunatech. All products were directly used without further purification.

2.2. Preparation of sc-SWCNT inks

To obtain printable sc-SWCNT inks, we dispersed 6 mg of SWCNTs in 10 ml toluene with 4 mg PFIID via probe-ultrasonication (Sonics & Materials, model: VCX 13 060 W) for 45 min. Then, it was centrifuged for 1 h at $15\,000$ rpm and $20\,800$ rpm, respectively, to remove the metal SWCNTs and insoluble matter. The resulting supernatant can be used directly in the manufacture of SWCNT TFTs or simply diluted to meet aerosol jet printing requirements.

2.3. Preparations of PBDB-T solution

The 10 mg PBDB-T was added to 5 ml of toluene and stirred with a magnetic stirring bar until completely dissolved. Finally, the PBDB-T solution was ready for use.

2.4. Fabrications of optoelectronic synaptic transistors

Al gate electrodes with a thickness of 150 nm were fabricated by standard photolithography, thermal vapor deposition, and lift-off processes on polyimide (PI) substrates. The 30 nm HfO_2 dielectric layer was then deposited on the gate electrodes by atomic layer deposition (ALD) technique (tetrakisdimethylamino hafnium and water as precursors, the growth temperature: ~ 150 °C). Next, the source and drain electrodes (150 nm Ag) were formed on the dielectric layer using the method described above. The sc-SWCNT ink was deposited into the device channels by Optomec aerosol jet printer (USA) and then annealed at 120 °C for 3 min. The excess polymer was removed from the device channels with toluene and then the

devices were annealed again. Eventually, the PBDB-T solution was spin-coated on the channels of SWCNT TFTs at 1000 rpm in an ambient atmosphere for 20 s.

2.5. Characterization and measurements

The absorbance spectra of PFIID-sorted sc-SWCNT inks were acquired using a UV-Vis-NIR spectrophotometer (Lambda 750, Perkin Elmer). The surface morphologies of the SWCNT networks were conducted by scanning electron microscopy (SEM, Nova NanoSEM450). Element composition and content were analyzed by x-ray Photoelectron Spectroscopy (XPS, Nano-X from Suzhou Institute of Nano-Tech and Nano-Bionics, PHI 5000 Versa probe II). Electrical characteristics of all SWCNT/PBDB-T TFT devices were recorded using the Keithley 2636B or Keithley 4200 electrometer system at room temperature. The equations of subthreshold swing (SS): $SS = \frac{dV_{GS}}{d(\log I_{DS})}$. The field effect mobilities were calculated using the standard linear regime: $\mu = 10^4 \times \frac{dI_{DS}}{dV_{GS}} \times \frac{L}{W} \times \frac{1}{C_{ox} V_{DS}}$. Here, C_{ox} is the HfO_2 dielectric capacitance per unit area, which is $0.06 \mu F \cdot cm^{-2}$ at 100 kHz (Measured by a Keithley 4200 electrometer system), as well as the L and W are the channel length ($5 \mu m$) and width ($150 \mu m$), respectively.

3. Result and discussion

Figure 1(a) schematically shows the manufacturing process for a PBDB-T-modified SWCNT synaptic transistor array with a bottom gate/bottom contact structure. As shown in figure 1(a), gate electrodes (150 nm Al) were grown on a PI substrate by the thermal evaporation, a 30 nm HfO_2 dielectric layer was produced by ALD, and Ag source and drain electrodes were deposited on the dielectric layer by the thermal evaporation. Sc-SWCNTs sorted by PFIID were used as channeling material deposited by the Aerosol Jet printer. As the light absorbing material, PBDB-T (chemical structure shown in figure S1) was spin-coated onto SWCNT TFT. Figures 1(b) and S2 show the photographs of a 20×10 SWCNT TFT array and the optical image of a single device in the array from the top view. Figure 1(c) is the structure diagram of the bottom-gate and bottom-contact SWCNT TFT. From figure 1(d), PBDB-T can be observed on the SWCNT thin film after spin coating compared with the original SWCNT thin film (figure S3). It is evident that sc-SWCNT thin films become blurred after being modified with PBDB-T, which demonstrates that the uniform PBDB-T films are deposited on the surfaces of the carbon nanotube films. In addition, to further verify the presence of PBDB-T, the XPS was used to characterize the SWCNT films before and after spin-coating. Figures 1(e) and (f) respectively present the XPS spectra for S1s and C1s of the above two samples. As shown in figure 1(e), the two peaks of S2p in the SWCNTs film after spin-coating with PBDB-T are located at 163 eV and 165 eV, respectively, while no peak of S1s is observed in the initial SWCNTs film. In addition, the C1s peak of SWCNT (284.6 eV) is shifted to a lower binding energy compared to that of SWCNT/PBDB-T (285.2 eV) as shown in

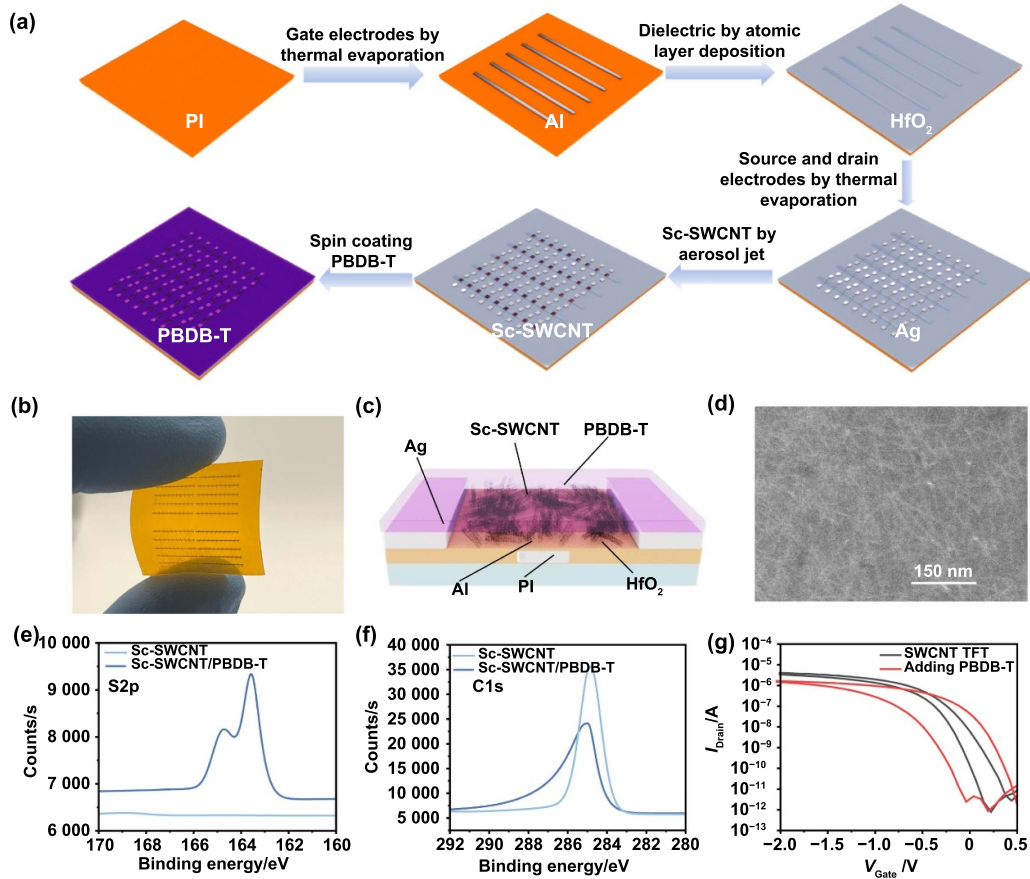


Figure 1. SWCNT/PBDB-T TFT device and material-related characterization. (a) Schematic diagram of the manufacturing process of SWCNT/PBDB-T TFTs. (b) The optical image of the SWCNT/PBDB-T TFT array. (c) The structure schematic diagram of the bottom-gate and bottom-contact SWCNT TFT device. (d) SEM image of SWCNT/PBDB-T deposited in the device channels. (e) S2p and (f) C1s XPS spectra of SWCNT thin films with or without PBDB-T. (g) The typical transfer curves of SWCNT TFT before and after modification with PBDB-T.

figure 1(f). The presence of S2p as well as the shifting of the C1s peaks confirms our hypothesis that the PBDB-T has been covered on the SWCNT films by spin-coating. The lines in figure 1(g) represent typical transfer curves of SWCNT TFTs before and after spin-coating PBDB-T, respectively. As can be seen from figure 1(g), the hysteresis of the spin-coated TFT is doubled, and the on-state current and threshold are changed, but the device still achieves a high switching ratio of 1×10^6 at a low operating voltage (-2 to 0.5 V). Subsequently, the electrical properties of the SWCNT/PBDB-T TFT arrays were further characterized. Figure S4 shows the transfer curves of the 20 transistors selected randomly and electrical performance parameters (the statistics of I_{On}/I_{Off} ratio, μ , SS, and their distributions) of the 50 transistors selected randomly at $V_{DS} = -0.25$ V, respectively, where the statistical results prove the device performance uniformity in high-performance SWCNT/PBDB-T TFTs. Clearly, the threshold voltage of the device is around 0.4 V and the I_{On}/I_{Off} ratio can reach 10^6 . In addition, the mobility of about $5.5 \text{ cm}^2 \text{ V}^{-1} \cdot \text{s}^{-1}$ can be achieved as well as the SS of 80 mV dec^{-1} . It should be emphasized that, as shown in figure S5, the prepared devices can still maintain good performance after bending.

As shown in figure 2(a), when sensory organs receive external stimuli, they first converts the different forms of physical stimuli into information-coded and brain-interpretable electrical signals. The presynaptic neuron receives a signal and releases neurotransmitters into the synaptic gap, while the receptors of the postsynaptic neuron receive the synaptic transmitter and undergo a change in signaling potential, generating a postsynaptic current. Conditions such as the number of presynaptic stimuli and stimulus duration modulate the strength of synaptic connections, defined as synaptic weights, which directly affect the postsynaptic current. Similar to the process of releasing neurotransmitters from the presynaptic membrane after receiving a signal to the postsynaptic membrane to achieve electrical signal transmission, when the synaptic transistor is stimulated by the gas or light, a large number of carriers enter the conductive channel to form excitatory postsynaptic currents (EPSCs), which are regulated by factors such as the width and number of external stimuli impulses.

Firstly, as shown in figure 2(b), we applied ten pulses of light (650 nm , $6 \text{ mW} \cdot \text{cm}^{-2}$, 0.5 s) and ten pulses of NO_2 gas (40 ppm , 5 s) respectively to achieve simple simulations of olfactory and visual synapses. It is important to note that

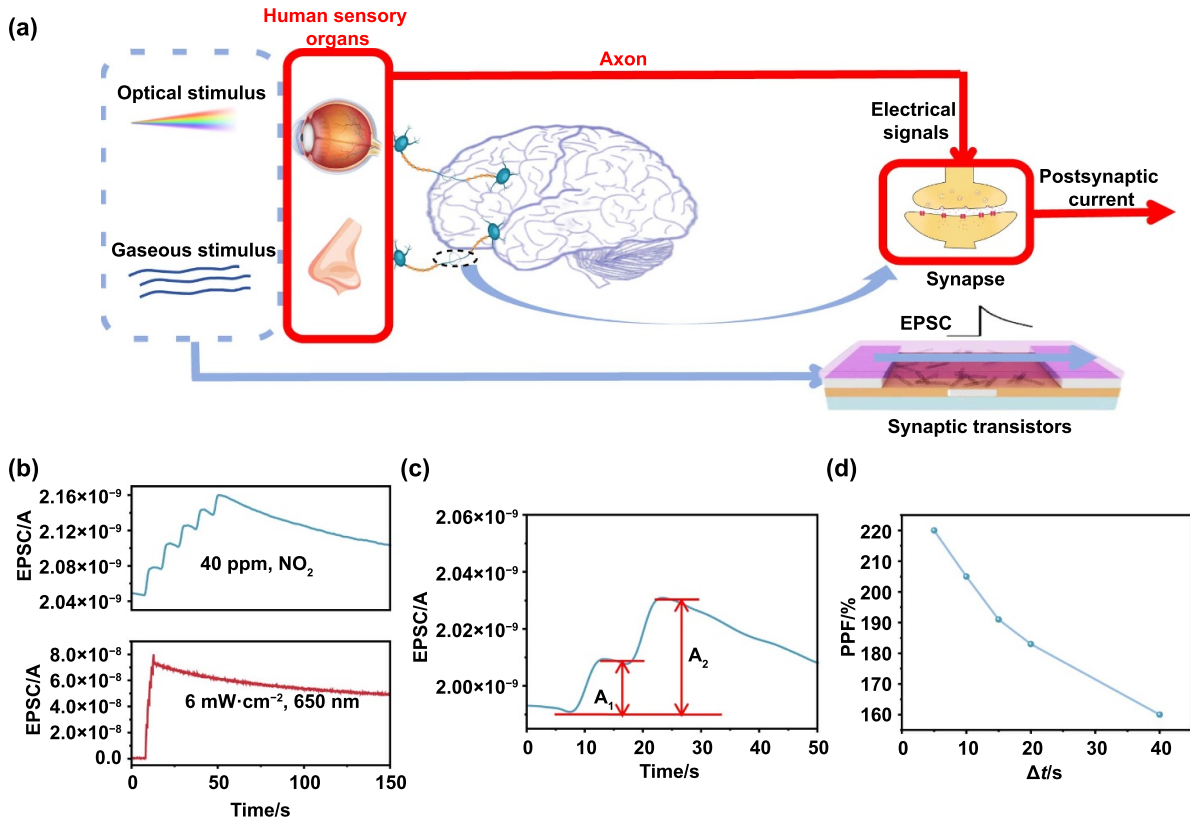


Figure 2. Schematic representation of olfactory-visual artificial synapses and tests of synaptic plasticity. (a) Schematic diagram simulating human olfactory and visual recognition of external information. (b) The EPSC excited by 10 light pulses (650 nm, $6 \text{ mW}\cdot\text{cm}^{-2}$, 0.5 s) and 10 NO₂ pulses (40 ppm, the Δt of 5 s), respectively. (c) The behavior of the PPF induced by two NO₂ pulses (40 ppm, 5 s, Δt of 5 s). (d) PPF index as a function of Δt . V_{DS} is -0.1 V and V_{GS} is 0.6 V in all the above experiments.

spin-coating PBDB-T did not affect the response of SWCNT to NO₂ (figure S6). Subsequently, we specifically investigated the synaptic behavior of individual senses. In biology, paired-pulse facilitation (PPF) is a typical expression of short-term plasticity (STP), which refers to the fact that when the synapse is stimulated to two adjacent pulses, two postsynaptic spikes are generated, and if the second spike is stronger than the first. As shown in figure 2(c), the PPF of the SWCNT/PBDB-T based device was successfully simulated by using two NO₂ pulses (40 ppm, the pulse width of 5 s and the time interval of 5 s), and the EPSC was read at a V_{DS} of -0.1 V and a V_{GS} of 0.6 V . The index of PPF is defined by the following equation:

$$\text{PPF index} = \frac{A_2}{A_1} \times 100\%$$

where A_1 and A_2 are the amplitudes of the first EPSC and the second EPSC, respectively. The PPF index induced by the NO₂ stimulus showed an exponential decrease with an increase in the time interval (Δt) between two pulses, with a maximum value of 220% (figure 2(d)).

In the human nervous system, two basic types of synaptic plasticity, STP and LTP, are thought to underlie learning and memory behavior. Synaptic plasticity transforms from STP to LTP when performing repetitive activities. Figure 3(a)

illustrates the EPSC characteristics triggered by different numbers of NO₂ pulses. As the number of pulses increased from 1 to 20, the triggered EPSC increased from $2.02 \times 10^{-9} \text{ A}$ to $2.27 \times 10^{-9} \text{ A}$ (figure 3(b)). In addition, the associated decay time increased at the same time, similar to the STP to LTP process. Also, as shown in figures 3(c) and (d), by adjusting the width of NO₂ pulses with the NO₂ concentration of 40 ppm, the synaptic properties can also be well regulated with peak EPSC values increasing from $2.03 \times 10^{-9} \text{ A}$ to $2.40 \times 10^{-9} \text{ A}$. Subsequently, the long-term retention responses of the NO₂ and synaptic behavior of SWCNT/PBDB-T TFTs were explained (figures 3(e) and (f)). As shown in figure 3(e), the gas response mechanism of SWCNTs was discussed based on the interaction of NO₂ molecules with SWCNTs. The detailed response process can be explained as follows: oxygen molecules first adsorb on the surface of SWCNTs and extract a large number of free electrons, thus producing chemisorbed oxygen species. Based on previous studies, the SWCNTs act as P-type semiconductors. When SWCNTs are exposed to NO₂ gas, NO₂ molecules can extract the electrons from SWCNTs. Therefore, due to the adsorption of NO₂ molecules, the concentration of holes in SWCNTs increases, resulting in an increase in current. Unlike conventional gas sensors, which revert to their original state once they are no longer exposed to the gas, the EPSC of

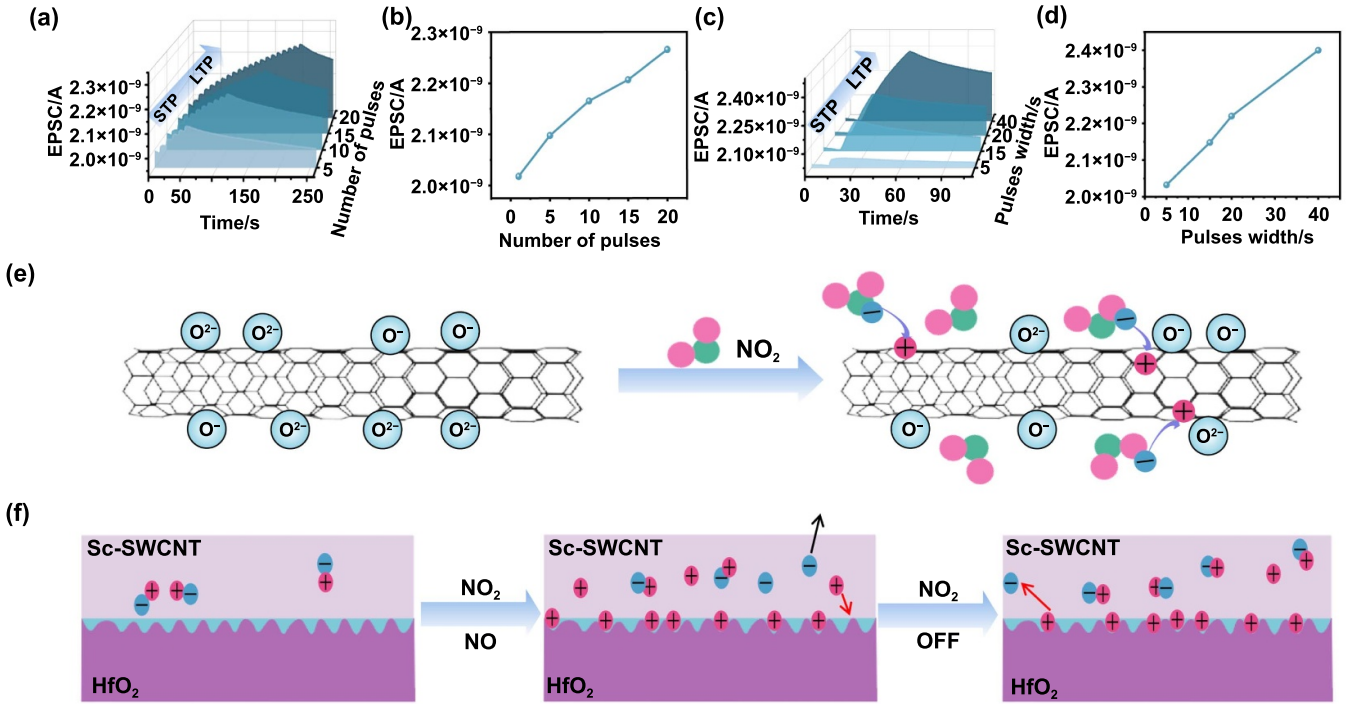


Figure 3. Effect of pulse number and pulse width on EPSC and related mechanisms. (a) The EPSC curves and (b) the maximum EPSC values with different numbers of gas pulses. (c) The EPSC curves and (d) the maximum EPSC values with different gas pulse widths. (e) The sensing mechanism of SWCNT TFT. (f) The illustration of the charge capture effect at the interface between the active and dielectric layers of an artificial synaptic TFT stimulated by pulsed NO₂.

SWCNT TFT can remain for a considerable period of time after the NO₂ pulses end. We attribute this to the defect states at the interface of the SWCNTs and HfO₂ [29]. As shown in figure 3(f), in the absence of NO₂, the transistor channel has only a few free carriers. When the device is exposed to NO₂, some of the holes are trapped by the defect states at the SWCNTs/HfO₂ interface, and most of the holes are not released at the end of NO₂ stimulation [30, 31]. In addition, as shown in figure S7, PBDB-T/SWCNT synaptic transistors also exhibit synaptic properties in response to NH₃ gas stimulation. However, in contrast to the response characteristics with the pulsed NO₂ stimulation, inhibitory postsynaptic currents were generated after NH₃ stimulation.

As shown in figure 2(b), the SWCNT thin-film transistor spin-coated with PBDB-T can achieve the simulation of synaptic behavior under the illumination of 650 nm wavelength light, which corresponds to the absorption spectrum of PBDB-T solution (figure 4(a)). As can be seen in figure 4(b), at the fixed -0.1 V of V_{DS} , the EPSC of SWCNT TFTs spin-coated with PBDB-T under stimulation with light pulses at 650 nm showed a great improvement, increasing from 1.95×10^{-9} A to 7.27×10^{-8} A, which was attributed to the synergistic correlation between the PBDB-T and SWCNT components. Figure 4(c) shows the transfer characteristics of the SWCNT/PBDB-T TFT device in the dark and under different wavelengths of light illumination. The transfer curves of the TFT shift to the positive direction and the on and off

currents of the device increase under light illumination at 280–650 nm as compared to the dark conditions, indicating the excellent response of the synaptic arrays in the visible light range.

To explain the mechanism of light response and synaptic behavior of SWCNT/PBDB-T TFT, the schematic band diagram of SWCNT/PBDB-T and the charge transfer between SWCNT, PBDB-T, and HfO₂ is described in detail below (figure 4(d)). As shown in figure 4(d), the highest occupied molecular orbital (HOMO) and lowest unoccupied molecular orbital (LUMO) energy levels of PBDB-T are -5.30 eV and -3.30 eV, respectively, according to the literature [32]. On the other hand, the valence band (VB = -4.15 eV) and conduction band (CB = -4.80 eV) energy levels of SWCNTs can be determined by the previous studies of the photoelectron energy spectra and additional optical band gap and exciton binding energies, respectively [33]. Light stimulation causes PBDB-T to produce exciton pairs. The defect states in HfO₂ trap most of the electrons under the influence of the gate voltage, while the remaining holes are transferred to the VB of SWCNT to participate in the conductivity, thus increasing the channel current [34–37]. The PPF behavior of the SWCNT/PBDB-T synaptic transistor stimulated by 650 nm wavelength light is shown in figure 4(e). It should be noted that the average PPF index increases as the wavelength decreases from 280 nm to 650 nm, indicating that optical pulses of longer wavelengths accelerate information processing (figure 4(f)).

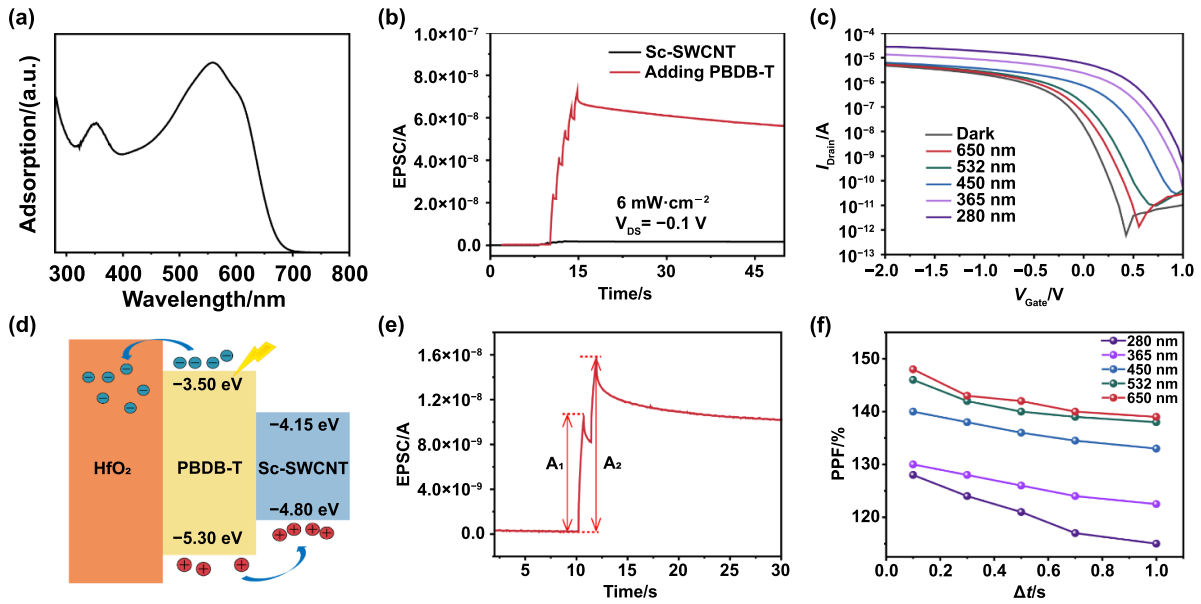


Figure 4. Photosynaptic characterization of PBDB-T/SWCNT TFT. (a) UV–Vis–NIR absorption spectrum of the PBDB-T solution. (b) The photoresponses of SWCNT TFT before and after spin-coating with PBDB-T. (c) Transfer characteristic curves of the SWCNT/PBDB-T synaptic transistor under dark conditions, and under light illumination of different wavelengths. (d) Schematic band diagram of SWCNT/PBDB-T and the charge transfer between SWCNT, PBDB-T, and HfO₂. (e) The behavior of the PPF induced by two light pulses (650 nm, 6 mW cm⁻², 0.5 s, the Δt of 0.5 s). (f) PPF index induced by the light pulses (6 mW·cm⁻², 0.5 s) with the wavelengths of 280 nm, 365 nm, 450 nm, 532 nm, and 650 nm as a function of Δt , respectively.

As shown in figure 5(b), similar to NO₂ synaptic behavior, the triggered EPSC increased with increasing pulse width (from 3.66×10^{-8} A to 1.55×10^{-7} A). In addition, as shown in figures 5(b) and (c), different pulse durations and frequencies also lead to different synaptic behaviors. It should be emphasized that modulation of synaptic plasticity can also be achieved by adjusting the wavelength of incident light from 280 nm to 650 nm (figures 5(d)–(f)). Among the four different wavelengths of photon pulses, the photon pulses with a wavelength of 280 nm excited the largest EPSC (50 pulses up to 7.34×10^{-7} A), while the photon pulses with a wavelength of 650 nm produced the smallest EPSC (50 pulses up to 1.70×10^{-7} A). Figure S8 shows that the power consumption per light pulse of the synaptic device is 25 aJ at the V_{DS} of 1×10^{-5} V. It must be emphasized the lower power consumption of our synaptic device compared to previously reported synaptic transistors [38–45] (figure 5(g)), which is more favorable for the further applications in AI. As shown in figures 5(h) and (i), the SWCNT/PBDB-T synaptic transistor operated normally in the temperature range of 0 ~ 150 °C with almost no attenuation of the optical response, proving the reliability of the device in extreme environments. As the temperature increased, the retention time of the EPSC decreased due to the fact that the carriers are more active at high temperatures and the holes and electrons are more readily recombination.

To solve this problem, we can take advantage of the temperature dependence of the barrier height to achieve excellent storage performance at high temperatures by constructing double-gate dielectric stacks or floating gate structures [46]. In addition, using ferroelectric dielectric materials with high

Curie temperatures can also improve the storage performance of devices at high temperatures [47]. It is obvious that the electrical properties of the devices show almost no degradation with increasing temperature (figure S9). In addition, it should be emphasized that thanks to the good stability of the SWCNT and PBDB-T, our devices were still stable after 40 d (figure S10). The results of our study are summarized in table S1 and compared with the critical characteristics (such as I_{ON}/I_{OFF} ratio, power consumption per pulse, and operating temperature) of recently reported synaptic devices, demonstrating that our proposed devices achieved high I_{ON}/I_{OFF} ratio ($>10^6$) and ultra-low power consumption (25 aJ) at low operating voltages (–2 to 1 V) in the operating temperature range of 0–150 °C.

Based on the synaptic plasticity of the device studied above, different EPSC values can be obtained by adjusting the optical pulse wavelength and optical pulse duration. In order to demonstrate the possibility of the device's application in optical information processing and optical wireless communication, we used presynaptic pulses representing Morse code to obtain the EPSC response corresponding to the English alphabet. As shown in figure 6(a), during the test period, 450 nm light was selected for stimulation, and the pulse widths of the short and long signals were set to 0.1 s and 0.5 s, respectively. The pulse intervals for the same letters were 1 s. It is clear that each letter exhibited a distinct EPSC amplitude response and the different letters produced EPSC curves with different profiles. In addition, when the pulse width is fixed at 0.5 s, optical pulses (450 and 650 nm) can be selected to represent short and long signals, respectively (figure 6(b)). As shown in figure 6(c), the synaptic weights extracted from the

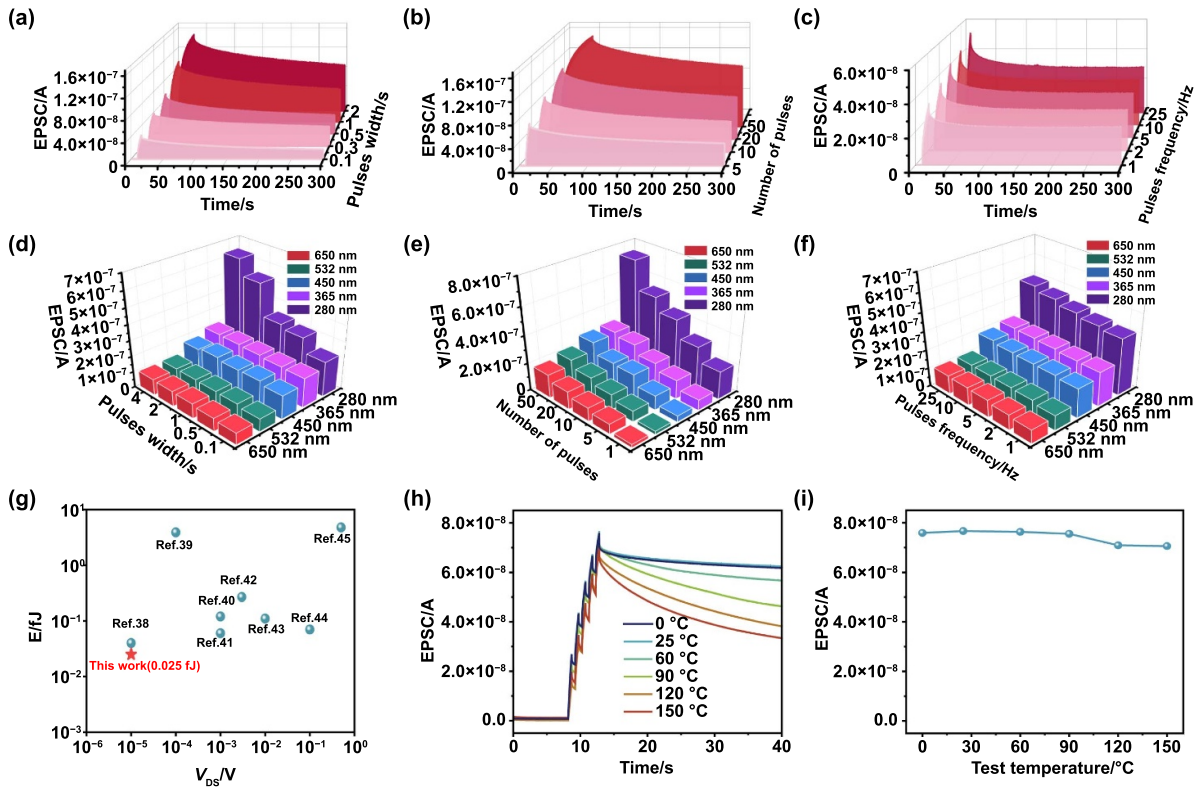


Figure 5. Photosynaptic characterization and stability of PBDB-T/SWCNT TFT. The EPSC under the light stimulation with different (a) pulse widths, (b) number of pulses, and (c) pulse frequencies. The maximum EPSC values with different (d) pulse widths, (e) number of pulses, and (f) pulse frequencies at various light wavelengths ($6 \text{ mW}\cdot\text{cm}^{-2}$, $V_{DS} = -0.1 \text{ V}$). (g) The statistics chart of reported synaptic transistor power consumption. (h) The EPSC curves and (i) the maximum EPSC values with different test temperatures.

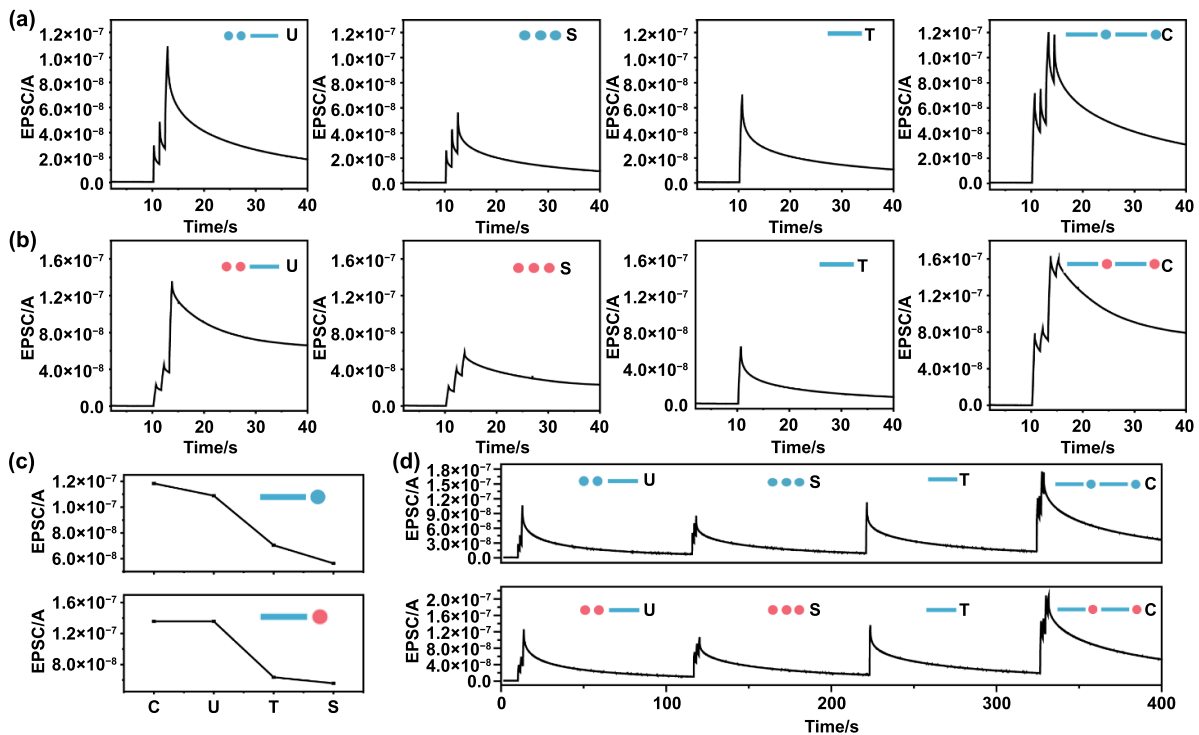


Figure 6. Morse code wireless optical communication. (a) The EPSC curves of Morse codes for letters U, S, T, and C triggered by different pulse widths (0.1 and 0.5 s). (b) The EPSC curves of Morse codes for letters U, S, T, and C triggered by different pulse wavelengths (650 and 450 nm). (c) The relationship between Morse code inputs and device outputs (The top graph represents different pulse widths; the bottom graph represents different wavelengths). (d) A series of photonic pulses induced EPSC simulating the Morse code of ‘USTC’.

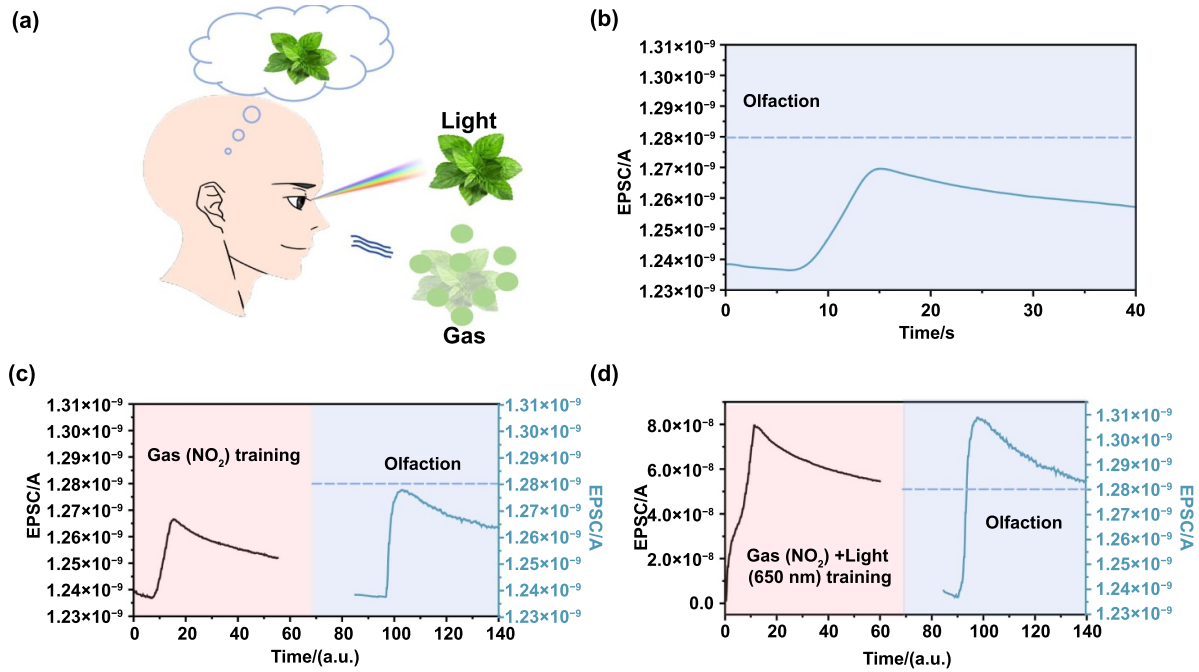


Figure 7. Olfactory-visual synergistic process simulation. (a) The schematic diagram of olfactory and visual multisensory collaboration. (b) The EPSC curve mimics olfactory dysfunction. The EPSC curves of simulated olfaction after (c) unimodal and (d) multimodal training.

EPSC curves were plotted as a correspondence between the device outputs and the Morse code inputs, where the letter C and the letter S excited to the maximum and minimum EPSC, respectively. As shown in figure 6(d), the device can decode the ‘USTC’ optical information by distinguishing the contours and peaks of the EPSC curves after combining different signals, and the peaks of the EPSCs of different letters were larger than those in figure 6(c), which may be due to synaptic learning and memory effects. The device can accurately respond to the ‘USTC’ coded information, which proved its great potential for application in the field of optical wireless communication.

Numerous studies have demonstrated a close link between olfaction and vision, and data suggest that the addition of the visual component to the olfactory system enhances olfactory neuroplasticity by stimulating cross-sensory transmission (figure 7(a)) [48–52]. In 2022, Khan *et al* reaffirmed this theory by comparing the efficacy of bimodal (visual-olfactory) training and unimodal (olfactory) training for COVID-19 postviral olfactory dysfunction. Subsequently, we modeled this process with our SWCNT/PBDB-T synaptic transistors. An EPSC value of 1.28×10^{-9} A was used as the threshold for normal olfaction. As shown in figure 7(b), the EPSC value was well below the threshold for normal olfaction after applying a single NO₂ pulse with a pulse width of 10 s, which can be used to simulate olfactory dysfunction induced by COVID-19 viruses [53]. We performed olfactory recovery training through both unimodal (olfactory) and bimodal (olfactory-visual) modalities. Unimodal training was performed by applying a single NO₂ pulse with a pulse width of 10 s. Two minutes later after training, we tested the olfactory recovery effect by applying the same pulse train as shown

in figure 7(b), and although the EPSC peak was elevated, it was still below the threshold for normal olfactory levels. In the bimodal experiments, the devices were simultaneously exposed to NO₂ gas and 650 nm light for 10 s. After two minutes, the peak of EPSC was well above the threshold level of normal olfactory sensation, demonstrating that bisensory synergism of olfactory-vision can be realized by our SWCNT/PBDB-T synaptic transistors.

4. Conclusion

In conclusion, we have developed a SWCNT/PBDB-T synaptic transistor array that not only has excellent electrical properties but also integrates olfactory (NO₂) and visual (from 280 nm to 650 nm) artificial synaptic functions on a single transistor for the first time, and realizes power consumption as low as 25 aJ for a single light pulse. The addition of a stable photosensitive material (PBDB-T) to the gas-sensitive SWCNT TFTs has realized a broad-spectrum response (from 280 nm to 650 nm) and a response to NO₂. In addition to mimicking typical synaptic behavior and exploring the transition of artificial synapses from STP to LTP, our neuromorphic device also successfully implemented wireless optical communication using Morse code and simulated the recovery of olfactory by bimodal training. The multimodal synaptic transistors demonstrated in this study can broaden the application scenarios of AI by introducing environmental interaction functions, and can also find applications in fields such as electronic robotic systems and neural prostheses.

Acknowledgment

Nianzi Sui and Kaixiang Kang contributed equally to this work. This work was supported by the National Key Research and Development Program of China (2020YFA0714700), Natural Science Foundation of China (62274174), Key Research and Development Program of Jiangsu Province (BK20232009), a fellowship from the China Postdoctoral Science Foundation (NO: 2023M742559) and the Cooperation Project of Vacuum Interconnect Research Facility (NANO-X) of Suzhou Institute of Nano-Tech and Nano-Bionics, Chinese Academy of Sciences (F2208). The authors are grateful for the technical support for Nano-X from Suzhou Institute of Nano-Tech and Nano-Bionics, Chinese Academy of Sciences (SINANO).

Credit authorship contribution statement

Nianzi Sui: Conceptualization, Methodology, Investigation, Formal analysis, Writing—original draft, Writing—review & editing. **Kaixiang Kang:** Conceptualization, Methodology, Investigation, Formal analysis, Writing—original draft. **Mi Li:** Writing—review & editing, Validation, Conceptualization. **Dan Zhang:** Methodology, Writing—review & editing. **Benxiang Li:** Writing—review & editing. **Shuangshuang Shao:** Investigation, Writing—review & editing. **Hua Wang:** Formal analysis, Writing—review & editing. **Jianwen Zhao:** Writing—review & editing, Validation, Conceptualization, Project administration, Funding acquisition.

Conflict of interest

The authors declare no competing financial interest.

ORCID iD

Jianwen Zhao  <https://orcid.org/0000-0002-5203-0143>

References

- [1] Merolla P A *et al* 2014 A million spiking-neuron integrated circuit with a scalable communication network and interface *Science* **345** 668–73
- [2] Schneider D 2018 U.S. supercomputing strikes back *IEEE Spectr.* **55** 52–53
- [3] Van De Burgt Y, Lubberman E, Fuller E J, Keene S T, Faria G C, Agarwal S, Marinella M J, Talin A A and Salleo A 2017 A non-volatile organic electrochemical device as a low-voltage artificial synapse for neuromorphic computing *Nat. Mater.* **16** 414–8
- [4] Laughlin S B, de Ruyter van Steveninck R R and Anderson J C 1998 The metabolic cost of neural information *Nat. Neurosci.* **1** 36–41
- [5] Ren Y, Yang J Q, Zhou L, Mao J Y, Zhang S R, Zhou Y and Han S T 2018 Gate-tunable synaptic plasticity through controlled polarity of charge trapping in fullerene composites *Adv. Funct. Mater.* **28** 1805599
- [6] Wang Y, Lv Z Y, Chen J R, Wang Z P, Zhou Y, Zhou L, Chen X L and Han S T 2018 Photonic synapses based on inorganic perovskite quantum dots for neuromorphic computing *Adv. Mater.* **30** 1802883
- [7] Jang S, Jang S, Lee E H, Kang M, Wang G and Kim T W 2019 Ultrathin conformable organic artificial synapse for wearable intelligent device applications *ACS Appl. Mater. Interfaces* **11** 1071–80
- [8] Wang Y, Yin L, Huang S J, Xiao R L, Zhang Y Q, Li D K, Pi X D and Yang D R 2023 Silicon-nanomembrane-based broadband synaptic phototransistors for neuromorphic vision *Nano Lett.* **23** 8460–7
- [9] Choudhry H H, Lee D H, Bag A and Lee N E 2023 A flexible artificial chemosensory neuronal synapse based on chemoreceptive ionogel-gated electrochemical transistor *Nat. Commun.* **14** 821
- [10] Wan H C, Zhao J Y, Lo L W, Cao Y Q, Sepulveda N and Wang C 2021 Multimodal artificial neurological sensory–memory system based on flexible carbon nanotube synaptic transistor *ACS Nano* **15** 14587–97
- [11] Wang S J *et al* 2023 An organic electrochemical transistor for multi-modal sensing, memory and processing *Nat. Electron.* **6** 281–91
- [12] Wu X M, Li E L, Liu Y Q, Lin W K, Yu R J, Chen G X, Hu Y Y, Chen H P and Guo T L 2021 Artificial multisensory integration nervous system with haptic and iconic perception behaviors *Nano Energy* **85** 106000
- [13] Wang Y R, Liu D X, Zhang Y M, Fan L C, Ren Q Q, Ma S H and Zhang M 2022 Stretchable temperature-responsive multimodal neuromorphic electronic skin with spontaneous synaptic plasticity recovery *ACS Nano* **16** 8283–93
- [14] Shen A M, Chen C L, Kim K, Cho B, Tudor A and Chen Y 2013 Analog neuromorphic module based on carbon nanotube synapses *ACS Nano* **7** 6117–22
- [15] Kim K, Chen C L, Truong Q, Shen A M and Chen Y 2013 A carbon nanotube synapse with dynamic logic and learning *Adv. Mater.* **25** 1693–8
- [16] Léonard F and Talin A A 2011 Electrical contacts to one- and two-dimensional nanomaterials *Nat. Nanotechnol.* **6** 773–83
- [17] Cao Q and Rogers J A 2009 Ultrathin films of single-walled carbon nanotubes for electronics and sensors: a review of fundamental and applied aspects *Adv. Mater.* **21** 29–53
- [18] Guo S Y, Hou P X, Zhang F, Liu C and Cheng H M 2022 Gas sensors based on single-wall carbon nanotubes *Molecules* **27** 5381
- [19] Jung S, Hauert R, Haluska M, Roman C and Hierold C 2021 Understanding and improving carbon nanotube-electrode contact in bottom-contacted nanotube gas sensors *Sens. Actuators B* **331** 129406
- [20] Liu F F, Xiao M M, Ning Y K, Zhou S Y, He J P, Lin Y X and Zhang Z Y 2022 Toward practical gas sensing with rapid recovery semiconducting carbon nanotube film sensors *Sci. China Inf. Sci.* **65** 162402
- [21] Xue L N, Wang W, Guo Y L, Liu G Q and Wan P B 2017 Flexible polyaniline/carbon nanotube nanocomposite film-based electronic gas sensors *Sens. Actuators B* **244** 47–53
- [22] Sun Y L, Li M J, Ding Y T, Wang H P, Wang H, Chen Z M and Xie D 2022 Programmable van-der-Waals heterostructure-enabled optoelectronic synaptic floating-gate transistors with ultra-low energy consumption *InfoMat* **4** e12317
- [23] Shao H *et al* 2023 A reconfigurable optoelectronic synaptic transistor with stable Zr-CsPbI₃ nanocrystals for visuomorphic computing *Adv. Mater.* **35** 2208497
- [24] Xie T H *et al* 2023 Carbon nanotube optoelectronic synapse transistor arrays with ultra-low power consumption for

- stretchable neuromorphic vision systems *Adv. Funct. Mater.* **33** 2303970
- [25] Chen Y T *et al* 2023 Bidirectional synaptic phototransistor based on two-dimensional ferroelectric semiconductor for mixed color pattern recognition *ACS Nano* **17** 12499–509
- [26] Brixi S, Melville O A, Boileau N T and Lessard B H 2018 The influence of air and temperature on the performance of PBDB-T and P3HT in organic thin film transistors *J. Mater. Chem. C* **6** 11972–9
- [27] Zheng Z, Yao H F, Ye L, Xu Y, Zhang S Q and Hou J H 2020 PBDB-T and its derivatives: a family of polymer donors enables over 17% efficiency in organic photovoltaics *Mater. Today* **35** 115–30
- [28] Abousamra W H, Thomas D, Yang D, Islam S M, Winstead C and Kim Y G 2023 Synthesis and characterization of the donor-acceptor conjugated polymer PBDB-T implementing group IV element germanium *Polymers* **15** 2429
- [29] Zhou C S, Zhao J W, Ye J, Tange M, Zhang X, Xu W W, Zhang K D, Okazaki T and Cui Z 2016 Printed thin-film transistors and NO₂ gas sensors based on sorted semiconducting carbon nanotubes by isoindigo-based copolymer *Carbon* **108** 372–80
- [30] Fang L, Dai S L, Zhao Y W, Liu D P and Huang J 2020 Light-stimulated artificial synapses based on 2D organic field-effect transistors *Adv. Electron. Mater.* **6** 1901217
- [31] Yang B *et al* 2020 Bioinspired multifunctional organic transistors based on natural chlorophyll/organic semiconductors *Adv. Mater.* **32** 2001227
- [32] Ren J P, Sun Y S, Huang S H, Huai Z X, Wang L X, Kong W G and Yang S P 2020 Broadening the light absorption range via PBDB-T to improve the power conversion efficiency in ternary organic solar cells *Org. Electron.* **78** 105587
- [33] Dass D 2018 Structural parameters, electronic properties, and band gaps of a single walled carbon nanotube: a p_z orbital tight binding study *Superlattices Microstruct.* **120** 108–26
- [34] Wang X, Yang S T, Qin Z Z, Hu B, Bu L J and Lu G H 2023 Enhanced multiwavelength response of flexible synaptic transistors for human sunburned skin simulation and neuromorphic computation *Adv. Mater.* **35** 2303699
- [35] Dai S L, Wu X H, Liu D P, Chu Y L, Wang K, Yang B and Huang J 2018 Light-stimulated synaptic devices utilizing interfacial effect of organic field-effect transistors *ACS Appl. Mater. Interfaces* **10** 21472–80
- [36] Hu D C, Yang R, Jiang L and Guo X 2018 Memristive synapses with photoelectric plasticity realized in ZnO_{1-x}/AlO_y heterojunction *ACS Appl. Mater. Interfaces* **10** 6463–70
- [37] Li H K, Chen T P, Liu P, Hu S G, Liu Y, Zhang Q and Lee P S 2016 A light-stimulated synaptic transistor with synaptic plasticity and memory functions based on InGaZnO_x-Al₂O₃ thin film structure *J. Appl. Phys.* **119** 244505
- [38] Li C H, Du W, Huang Y X, Zou J H, Luo L Z, Sun S, Govorov A O, Wu J, Xu H X and Wang Z M 2022 Photonic synapses with ultralow energy consumption for artificial visual perception and brain storage *Opto-Electron. Adv.* **5** 210069
- [39] Liu D P, Shi Q Q, Dai S L and Huang J 2020 The design of 3D-interface architecture in an ultralow-power, electrospun single-fiber synaptic transistor for neuromorphic computing *Small* **16** 1907472
- [40] Hao D D, Chen T Q, Guo P, Liu D P, Wang X, Huang H, Huang J, Shan F K and Yang Z Y 2023 Artificial optoelectronic synaptic devices based on vertical organic field-effect transistors with low energy consumption *Adv. Compos. Hybrid Mater.* **6** 129
- [41] Liu G C *et al* 2022 Ultralow-power and multisensory artificial synapse based on electrolyte-gated vertical organic transistors *Adv. Funct. Mater.* **32** 2200959
- [42] Cho S I, Jeon J B, Kim J H, Lee S H, Jeong W, Kim J, Kim G, Kim K M and Park S H K 2021 Synaptic transistors with human brain-like fJ energy consumption via double oxide semiconductor engineering for neuromorphic electronics *J. Mater. Chem. C* **9** 10243–53
- [43] Shi Q Q, Liu D P, Hao D D, Zhang J Y, Tian L, Xiong L Z and Huang J 2021 Printable, ultralow-power ternary synaptic transistors for multifunctional information processing system *Nano Energy* **87** 106197
- [44] Shi J L, Jie J S, Deng W, Luo G, Fang X C, Xiao Y L, Zhang Y J, Zhang X J and Zhang X H 2022 A fully solution-printed photosynaptic transistor array with ultralow energy consumption for artificial-vision neural networks *Adv. Mater.* **34** 2200380
- [45] Zhu C G *et al* 2022 Optical synaptic devices with ultra-low power consumption for neuromorphic computing *Light Sci. Appl.* **11** 337
- [46] Mroczynski R, Taube A, Gierałowska S, Guziejewicz E and Godlewski M 2012 Application of deposited by ALD HfO₂ and Al₂O₃ layers in double-gate dielectric stacks for non-volatile semiconductor memory (NVSM) devices *Appl. Surf. Sci.* **258** 8366–70
- [47] Tang W H *et al* 2022 A van der waals ferroelectric tunnel junction for ultrahigh-temperature operation memory *Small Methods* **6** 2101583
- [48] Kawase T, Sakamoto S, Hori Y, Maki A, Suzuki Y and Kobayashi T 2009 Bimodal audio-visual training enhances auditory adaptation process *NeuroReport* **20** 1231–4
- [49] Gottfried J A and Dolan R J 2003 The nose smells what the eye sees: crossmodal visual facilitation of human olfactory perception *Neuron* **39** 375–86
- [50] Olofsson J K, Ekström I, Lindström J, Syrjänen E, Stigsdotter-Neely A, Nyberg L, Jonsson S and Larsson M 2020 Smell-based memory training: evidence of olfactory learning and transfer to the visual domain *Chem. Senses* **45** 593–600
- [51] Jiramongkolchai P *et al* 2021 Association of olfactory training with neural connectivity in adults with postviral olfactory dysfunction *JAMA Otolaryngol Head Neck Surg.* **147** 502–9
- [52] Saatci O, Altundag A, Duz O A and Hummel T 2020 Olfactory training ball improves adherence and olfactory outcomes in post-infectious olfactory dysfunction *Eur. Arch. Oto-Rhino-Laryngol.* **277** 2125–32
- [53] Khan A M, Piccirillo J, Kallogjeri D and Piccirillo J F 2023 Efficacy of combined visual-olfactory training with patient-preferred scents as treatment for patients with COVID-19 resultant olfactory loss: a randomized clinical trial *JAMA Otolaryngol. Head Neck Surg.* **149** 141–9